



# Chapter 7

## Characterization and Modeling of Low Modulus Composite Patched Aluminum Center Crack Tension Specimen Using DIC Surface Displacements

Daniel C. Hart and Hugh A. Bruck

**Abstract** Composite patch repairs of aluminum structures used in marine and aerospace industries are designed using closed form solutions assuming thin, plane stress, linear-elastic structures or numerical methods for repairs of thick aluminum. Both methods are based on linear elastic fracture mechanics and compare crack tip predictions to a critical strain energy release rate or stress intensity. Analytical and numerical predictions are reasonable for linear-elastic behavior, but these methods do not account for elastic-plastic behavior at the crack tip that initiates above the linear-elastic limit and continues until the ultimate load. This research used digital image correlation and finite element analysis to study the full field displacement and J-integral ahead of the crack tip for un-patched and patched center crack tension specimens loaded monotonically to failure. Free surface crack tip strain and J-integral behavior remained an intrinsic property of the aluminum directly related to the crack opening displacement (COD) and were independent of one sided composite patch reinforcement. However, the crack tip bending deformations induced by the patch reinforcement increased the COD by 20% over the un-patched behavior after patch failure, most likely due to observed changes in the formation of the plastic zone ahead of the crack. Comparison of test results and analytical predictions indicated a significant difference between linear elastic and elastic plastic predictions beyond the linear-elastic limit highlighting the need to utilize elastic plastic fracture mechanics and the J-integral to optimize composite patched center crack tension specimens for ultimate load.

**Keywords** Composite patch · Aluminum · Digital image correlation · J-integral · Center crack tension

### 7.1 Introduction

The foundation of bonded joint design started in the late 30's and 40's with the governing differential equations for an explicit adhesive layer [1, 2], and later advanced when Hart-Smith added inelastic behavior of that adhesive layer [3, 4]. In application, the development of aircraft patch repairs continued through a combination of mechanical characterization protocols, development of appropriate design methods based on using the governing equations with mechanical characterization data, and enhancement of analysis efforts [5–9] by incorporating linear elastic fracture mechanics (LEFM) to calculate strain energy release rate (SERR) or stress intensity (K) at the metallic crack tip. When designing composite patch repairs for aluminum, using LEFM results in a conservative design. As the thickness of the repaired plate increases and the loading increases, the failure mechanisms and energies not captured by the existing analyses begin to play significant roles in the ultimate in-plane static tensile load capacity of the repaired region. From the initial research into 2D bonded joints, it was assumed the dominant energy dissipation mechanism was the plastic deformation of the adhesive layer. When extending the design approach for 2D joints to include the crack tip of composite patched aluminum repairs, Wang and Rose utilized a distribution of springs to represent the adhesive and plate theory for the in a linear elastic energy balance for a bending deformation analysis in order to predict crack tip stress intensity using Rose's model [10]. Advancements in computational algorithms, particularly Finite Element Analysis techniques such as Virtual Crack Closure, simplified development of numerical analysis approaches [11–13]. However, neither the analytical or numerical methods incorporated elastic-plastic aluminum behavior at the crack tip in design.

---

D. C. Hart (✉)  
Naval Surface Warfare Center, Carderock Division, West Bethesda, MD, USA  
e-mail: [daniel.c.hart@navy.mil](mailto:daniel.c.hart@navy.mil)

H. A. Bruck  
University of Maryland Mechanical Engineering Department, College Park, MD, USA

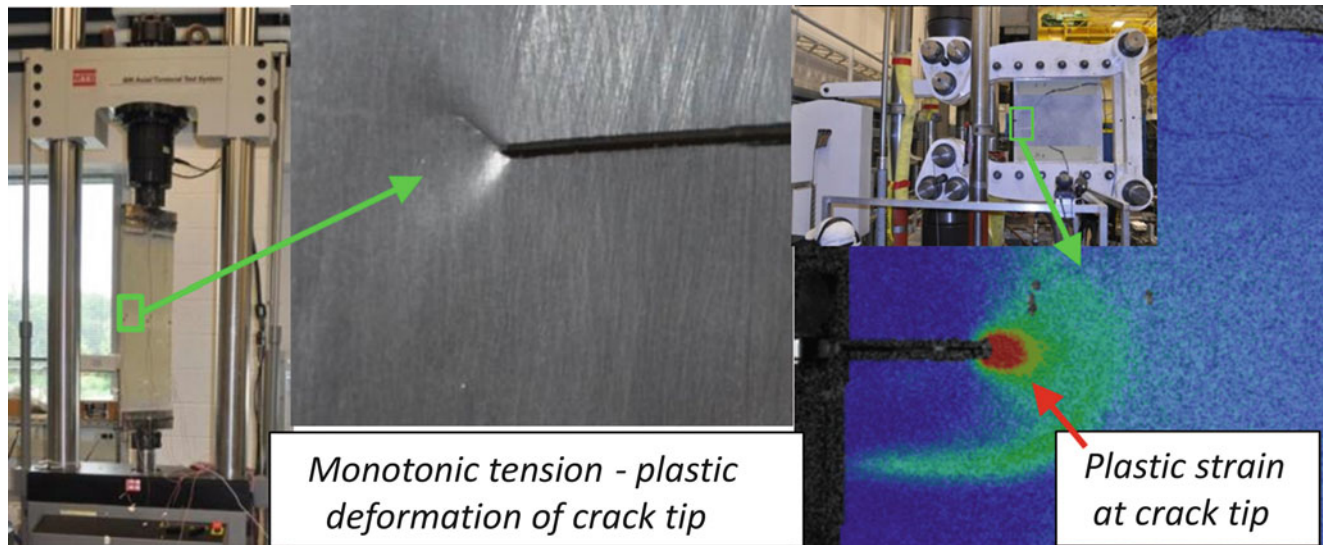


**Fig. 7.1** Plastic zone on free surface of large scale patched CCT (L) and ductile tearing (R) specimens

Recent testing of low modulus composite patches on center crack tension (CCT) specimens and a large scale ductile tearing specimen [14–16] have demonstrated significantly more monotonic load capacity of composite patched specimens than un-patched specimens. One of the common failure mechanisms observed which had not been accounted for was significant plastic deformation of the aluminum ahead of the crack tip. Large scale testing of one sided patched aluminum specimens, shown in Fig. 7.1, has shown that the elastic-plastic crack tip behavior occurs before ultimate failure with each patched specimen achieving higher load capacity and greater displacement capacity at failure [11, 14]. The J-integral method developed by Hutchinson, Rice, and Rosengren [17–19] established a measure of the non-linear behavior of the strain energy release rate for ductile metals. To characterize this behavior, Digital Image Correlation (DIC) [20] has been utilized to measure full field surface displacements ahead of the crack tip required to calculate the J-integral value. Initially utilized for linear elastic material behavior [21, 22], inelastic material behavior measured on the surface can be included in the J-integral calculation [23–25]. Research in the plastic zone development under monotonic loading appears to be limited to typical fracture mechanics metallic specimens of a single material [26, 27].

In this paper the focus will be on the effect one sided adhesively bonded low modulus E-Glass/Epoxy composite patch has on development of the crack tip plastic zone and evolution of the J-integral value for cracked aluminum CCT specimens loaded monotonically in tension until failure. Full field 2D DIC data from the un-patched, free, aluminum surface and J-integral calculations will be compared with LEFM and elastic plastic fracture mechanics (LEFM) based J-integral calculations and finite element analysis (FEA) based predictions to improve our understanding of the effect one sided surface reinforcement has on crack tip material behavior. This research looked at the aluminum crack tip behavior and does not currently address non-linear behavior of the adhesive layer or failure of the composite adherend. Low modulus composite patches were selected based on current U.S. Navy use of composite patch repairs to address cracking in sensitized aluminum plate [11, 14, 28, 29].

## 7.2 J-Integral Using DIC

The foundation of this investigation is the ability to gather full field displacement data ahead of and around the crack tip using 2D DIC. Images of the applied speckle pattern are processed to correlate patterns of gray scale values in specific square subsets between the initial reference image and deformed images [20]. Behavior between the reference frame and each image is approximated by optimizing polynomial coefficients of shape functions such that the squared difference between the pixel subset gray scale values of the image and the assumed values based on the shape functions is minimized. These optimized shape functions can then be used to calculate the displacements and displacement gradients necessary to get the Lagrangian strains. Shape functions are used to get results at the centroid of the subset. Results are stored at each subset offset in the horizontal (U) and vertical (V) directions defined by the step size. For the data reported square subset size was 51 pixels

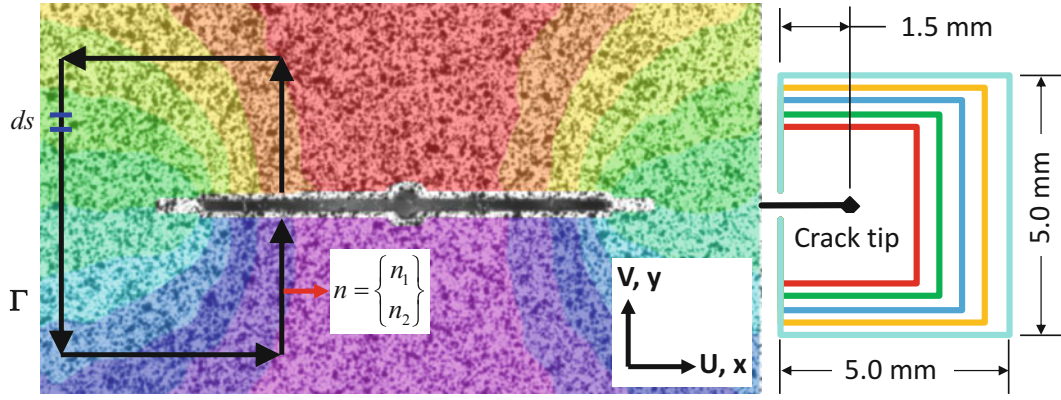


**Fig. 7.2** Vertical displacement fields with J-integral path example

(0.35 mm) with results stored every 10 pixels (0.07 mm). Strain results were filtered across 41 data points and then smoothed using the center-weighted Gaussian filter. Processing was performed using the commercially available Correlated Solutions (Irmo, SC) software, Vic2D, and the images taken during the monotonic tensile loading of the CCT specimens. Vic2D output displacements, displacement gradients, and strains. DIC data is limited to one side of the CCT specimen for this test series and can only provide material behavior information directly at the surface. Images were captured with a monochromatic complimentary metal-oxide semiconductor (CMOS) sensor with 4096x2160 pixel resolution.

The J-integral is a path independent contour integral that describes the non-linear strain energy release rate for elastic-plastic materials. The formulation of J assumes a 2D state at the crack tip, in other words plane strain or plane stress. In the case of surface measurements one must assume plane stress for the infinitesimal slice of material at the surface with no ability to infer the stress-strain behavior through the thickness from those measurements. The J-integral developed by Hutchinson, Rice, and Rosengren is shown below:

$$J = \int_{\Gamma} \left( w dy - T_i \frac{\partial u_i}{\partial x} ds \right) = \int_{\Gamma} \left( \int_0^{\epsilon_{ij}} \sigma_{ij} d\epsilon_{ij} dy - \sigma_{ij} n_j \frac{\partial u_i}{\partial x} ds \right) \quad (7.1)$$

Here  $w$  is the strain energy density,  $T_i$  is the traction vector normal ( $n_j$ ) to the path  $\Gamma$  with infinitesimal segments along that path ( $ds$ ). Displacements ( $u_i$ ) and strains ( $\epsilon_{ij}$ ) along the path and displacement data are located in  $xy$  space, such that  $i$  is associated with the  $x$ -direction and  $j$  is associated with the  $y$ -direction. From the DIC data processing  $U$  and  $V$  are in the  $x$  and  $y$ -directions respectively. Figure 7.2 shows the processed vertical displacement fields ( $V$ ) with J-integral path variables. Five paths were evaluated about the crack tip. Each square path starts 1.5 mm behind the crack tip and vary from 3 mm to 5 mm.

Assuming, for data processing simplification, that the surface material along the path is outside the crack tip plastic zone and behaves linear elastically the J-integral equation can be derived as a function of material parameters and the displacement gradients along the path  $\Gamma$  measured by DIC. As reported by Bruck [21], the J-integral value for elastic material becomes:

$$J = \frac{G}{2} \int_{\Gamma} \left[ \left\{ k_1 \left( \frac{\partial v}{\partial y} - \frac{\partial u}{\partial x} \right) \left( \frac{\partial u}{\partial x} + \frac{\partial v}{\partial y} \right) + \left( \frac{\partial u}{\partial y} + \frac{\partial v}{\partial x} \right) \left( \frac{\partial u}{\partial y} - \frac{\partial v}{\partial x} \right) \right\} dy + \left\{ 2 \left( \frac{\partial u \partial u}{\partial x \partial y} + k_2 \frac{\partial u \partial v}{\partial x \partial x} + k_1 \frac{\partial v \partial v}{\partial x \partial y} \right) \right\} dx \right] \quad (7.2)$$

Here the  $k_i$  values are defined, for plane stress, by the Poisson's ratio of the cracked material.

$$plane \ stress : k_1 = \frac{2}{1 - \nu}, k_2 = \frac{1 + \nu}{1 - \nu} \quad (7.3)$$

### 7.3 Experimental Configuration

The test frame, DIC setup, typical speckle pattern, and specimen configuration are shown in Fig. 7.3. Small scale CCT specimen geometry was selected for manufacturing and testing convenience as well as maintaining a configuration link to the large scale testing performed by Hart et al. [11, 16]. Aluminum selected for the small scale CCT specimens was based on

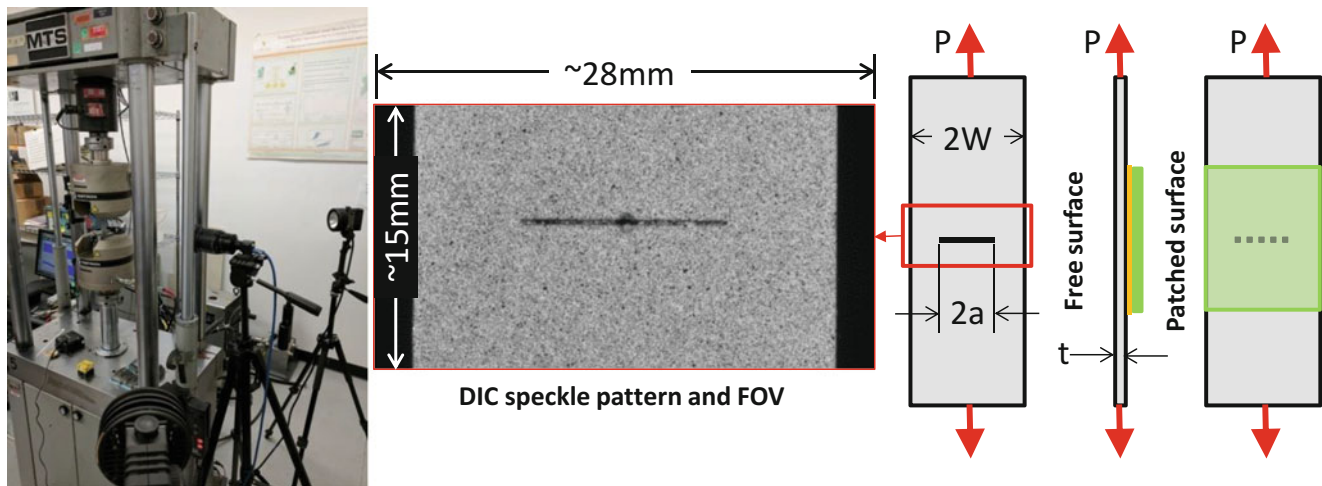


**Fig. 7.3** Small scale CCT test frame and DIC configuration (L), FOV (C), and CCT specimen geometry (R)

readily available plate thickness that allowed a nominally 1/3rd scale from the large scale specimens. A marine grade 5052-H32 aluminum was selected at 2.29 mm (0.090 in. thick, the typical 6.35 mm (0.25in) 5456-H116 was not readily available at that thickness. Small scale CCT specimen blank plates were 24 mm wide ( $2W$ ) and 114 mm long with electrical discharge machined (EDM) notches nominally 12 mm wide and nominally 0.36 mm high. Cracks were then grown from the notch to develop sharp crack tips using high cycle low load tension-tension fatigue. To grow the cracks the load ratio was 0.1 for a tensile load that varied from 200-2000 N at 10 Hz. The resulting effective  $\Delta K$  was nominally between 5.6 and 6.7 MPa- $\sqrt{\text{m}}$ , which resulted in a nominal cycle count of 100 K to achieve crack growth of approximately 1 mm. With sharp crack tips and a crack length ( $2a$ ) of 14 mm the specimens were paired by crack length and one of each pair received an adhesively bonded composite patch. Surface preparation involved an acetone wipe, light surface abrasion with 80 grit aluminum oxide sandpaper, another acetone wipe, and treatment with 3 M's AC-130-2 bonding agent. A commercially available marine adhesive, West Systems WestSix10, was selected for bonding the pre-fabricated 0/90 E-Glass epoxy laminate. The laminate had an average thickness of 1.27 mm (0.05 in. and was cut to 50 mm long by 24 mm wide. The composite patch was centered on the machined notch and bonded to the cracked aluminum plate with a nominally 0.6 mm thick bondline, which was controlled using 0.024 inch diameter steel welding wire.

Tensile testing was performed on a 20 kip 4-post hydraulic MTS frame with Instron hydraulic wedge grips and controls. Specimens were adapted to the wedge grips with temporarily bonded tabbing; the wedge grips had a minimum grip thickness of 7.8 mm and a 45 mm grip width. Care was taken to install the test specimens such that the edge was vertical to ensure the applied tensile load was perpendicular to the notch. Loading was applied at a rate of 0.18 mm/min until beyond the linear elastic response range when the non-linear load response slope stabilized in the crack blunting region. As crack blunting and plastic deformation began at the crack tip the load rate was doubled.

Images for DIC were taken using a Point Grey Flea FL3-U3-88S2C-C with a Tamron 28-80 mm f/3.5-22 lens resulting in a 28.2 mm  $\times$  14.9 mm overall field of view (FOV). Initial depth of field (DoF) was set such that the initial unloaded surface was at the extreme edge of focus. This provided enough DoF such that the surface remained in focus as load was applied and out of plane deflection decreased the distance between the specimen and the camera. The speckle pattern was achieved using a base of flat white spray paint with light passes of flat black spray paint. To achieve the smallest consistent speckles an improvised paint booth was fogged with black spray, then the specimen was placed in the space for the small floating paint particles to settle on the white surface. This process was repeated until sufficient gray scale information was present in the image. High contrast images were achieved using two evenly spaced 250 watt halogen spot lights; lights were equidistant from the grip bodies, equidistant to the camera body, and level with the camera body and specimen. During the linear elastic response range images were taken at 2 per second, as the response advanced into the crack blunting range the image rate was decreased then increased to the original speed prior to crack growth and failure.



### 7.4 Test Results

The initial data reported in this paper is limited to 2 un-patched and 2 patched specimens. Load versus crack opening displacement (COD) response due to monotonic tensile loading shown in Fig. 7.4 indicates consistent behavior between like specimens. DIC images were studied to match visual behavior with progression of the crack tip from linear elastic response, crack blunting, then finally crack growth until specimen failure. Load response combined with labels for the crack stage progression are shown in Fig. 7.4 and the DIC measured Von Mises strain ahead of the crack tip versus COD is shown in Fig. 7.5. The data indicates the transition of the fracture behavior on the free surface for both patched and un-patched specimens occurs at the same COD magnitudes. In other words, crack blunting for both un-patched and patched specimens occurs from just beyond the elastic limit until a critical COD limit of approximately 0.6 mm is reached, although the load required to achieve that COD is more than 100% greater for the patched specimen because of the load transfer to the patch that constrains the deformation of the free surface. The patched specimens exhibited visual evidence during crack growth that

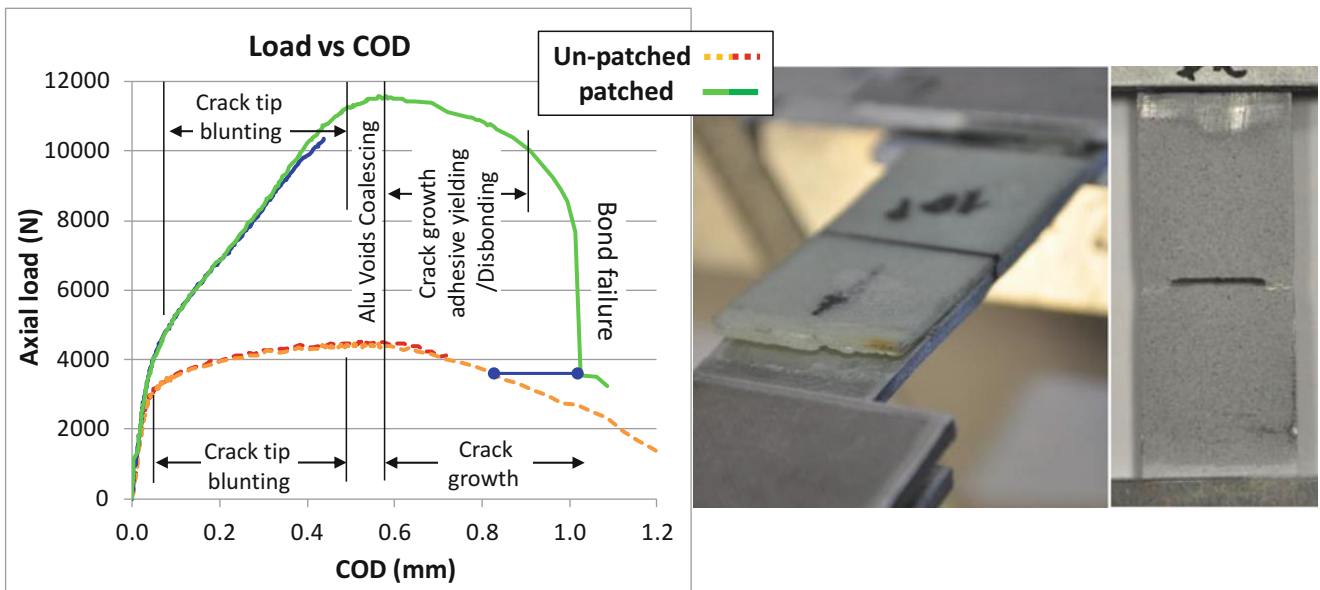


Fig. 7.4 Load versus crack opening displacement and a tested patched (L) and un-patched (R) specimen

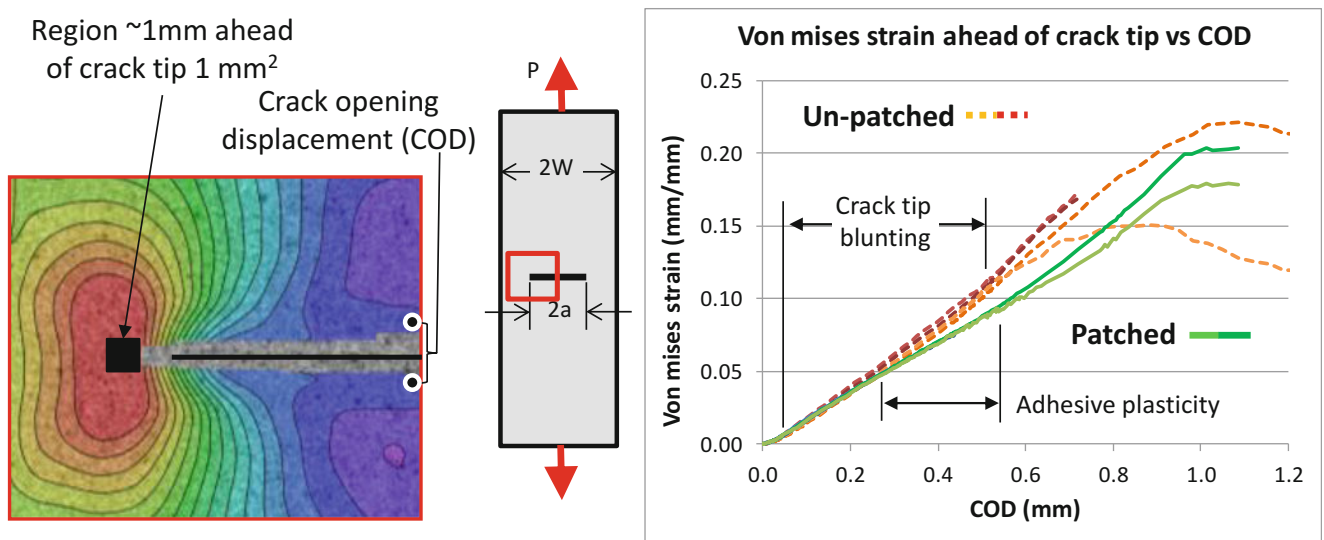
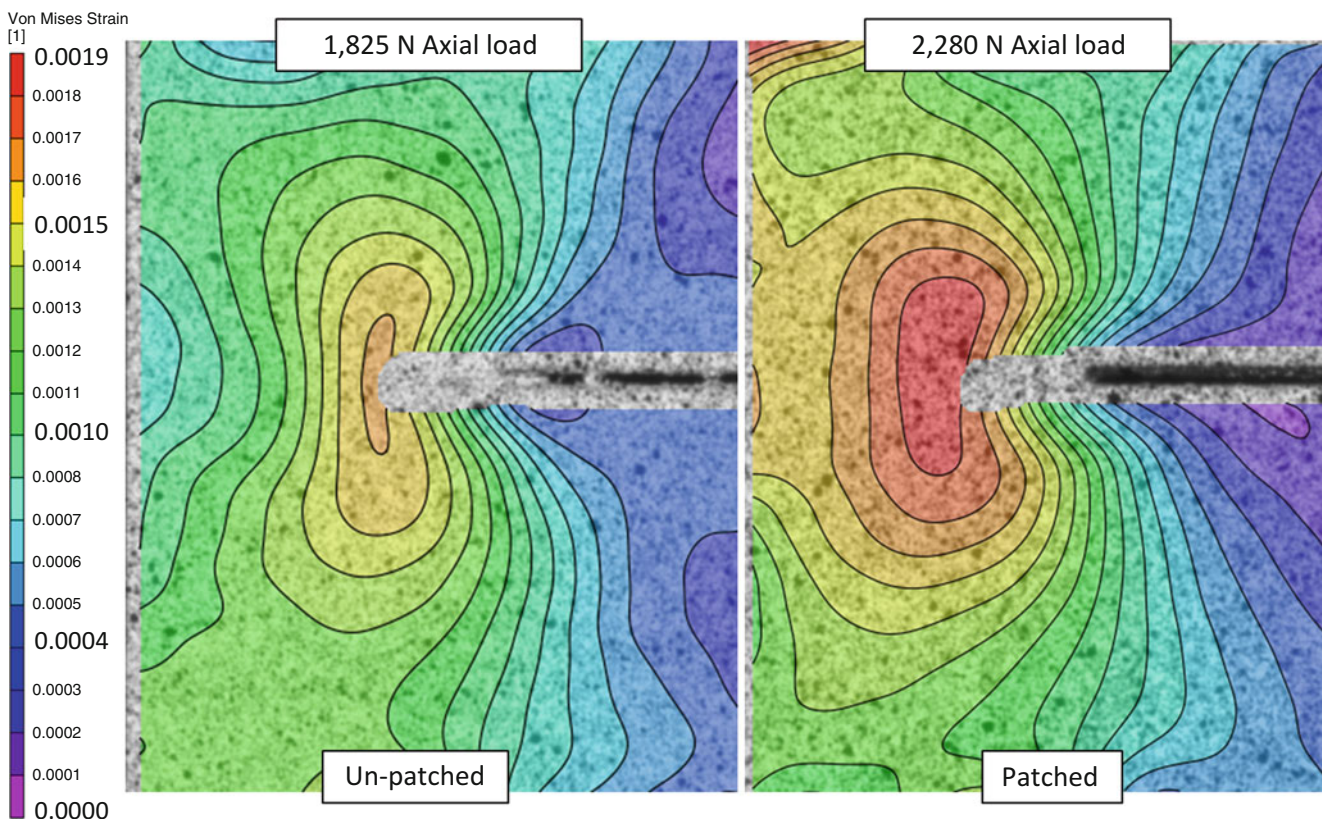


Fig. 7.5 Von Mises strain data ahead of the crack tip

suggests adhesive failure begins to occur after the peak load is achieved, thereby reducing the load transfer to the patch and the overall load-bearing capacity of the specimen. Failure of the adhesive continues until bond failure of half the patch (one side of the notch) where the crack growth behavior is then controlled by the fracture behavior of the aluminum. When comparing aluminum fracture at 3500 N, the load level after patch failure, the COD is 20% greater for the patched specimen shown by the blue line in Fig. 7.4. This additional 0.2 mm of COD on the free surface is related to the increased size and behavior of the plastic zone ahead of the crack tip for the patched specimen.

When comparing free surface behaviors of un-patched and patched specimens as a function of COD, the strain behavior ahead of the crack tip correlate reasonably well to the end of crack tip blunting, meaning the strain response on the free surface of the aluminum is nominally an intrinsic behavior of the material. Though the local crack tip behavior correlates with COD, the load required to achieve the same COD is significantly larger with the addition of the composite patch on the opposite surface, as previously discussed. In Fig. 7.5, the Von Mises strain behavior is plotted as a function of COD. The strain values plotted are averaged over a  $1 \text{ mm}^2$  region nominally 1 mm ahead of the crack tip; the distance ahead of the crack varied from 0.8 to 1.2 mm based on the defined area of interest in the DIC software. The area of interest was refined to exclude the crack plane such that failure to correlate image subsets later in the failure progression was minimized. This prevented detailed surface displacement data from being obtained directly at the edge of the crack plane. Average strain magnitude response ahead of the crack tip is the same for both patched and un-patched specimens until approximately 0.25 mm of COD. Here there is a change in the load versus COD as well as strain versus COD responses. This is presumed to be related to increase in the region of peak plastic shear stress in the adhesive allowing higher rate of load increase. As crack blunting transitions to crack growth the aluminum specimens exhibit tearing and a gradual drop in load as COD increases. The composite patched specimens indicate visual evidence of adhesive yielding. As COD is increased, visual evidence indicates bondline failure with large relative displacement between the patch and upper notch edge resulting in a large load drop. Once the composite patch bond fails, failure behavior of the patched specimen matches the load response of the aluminum specimens but with a larger magnitude of COD, as previously discussed.

At low magnitudes of COD, below 0.02 mm, the load versus COD response of the specimen is linear elastic. Von Mises strain contours in Fig. 7.6 are similar with the composite patched specimen showing a higher magnitude and larger region of high strain. This is due to the out-of-plane bending, in the linear elastic region the bending increases until the load passes



**Fig. 7.6** Von Mises strain contour comparison for a COD = 0.02 mm in the linear elastic range



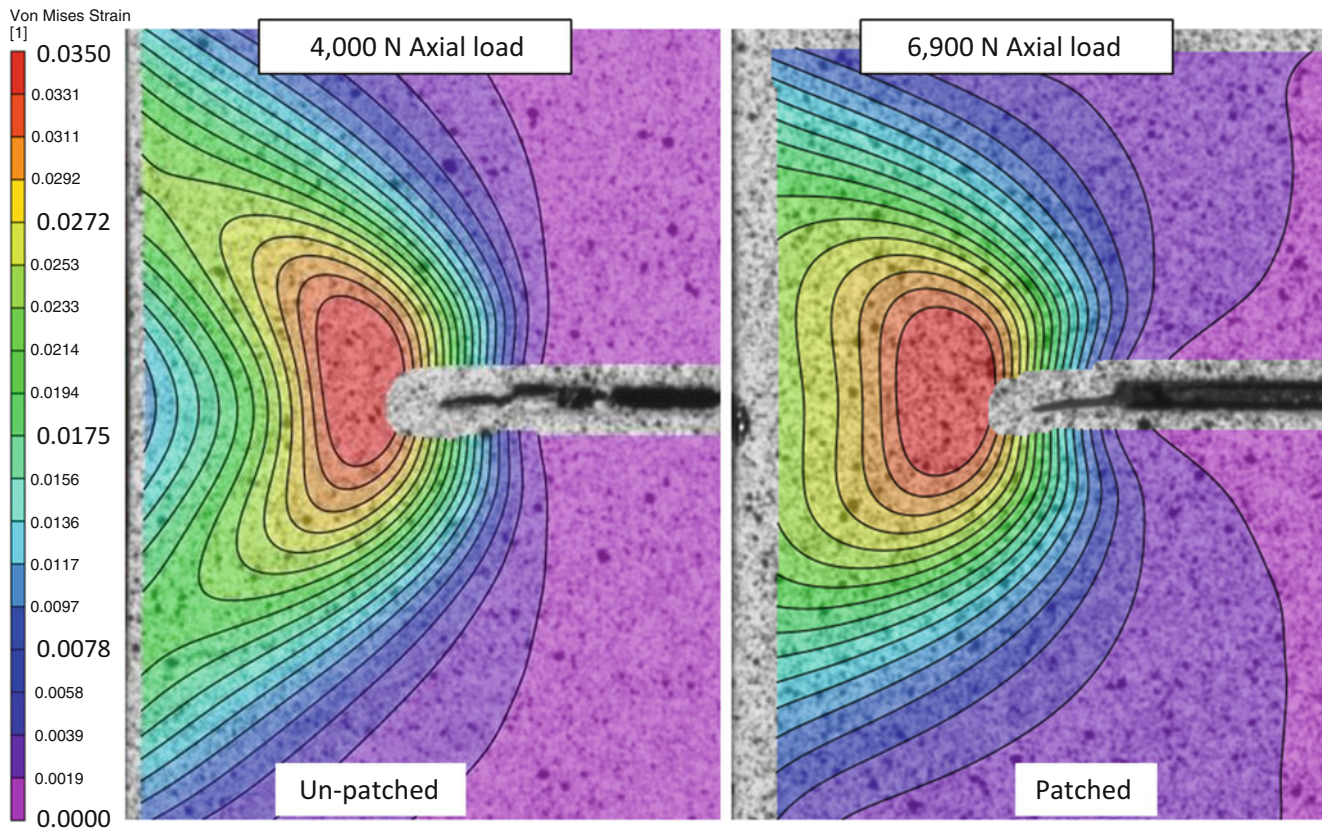


**Fig. 7.7** Von Mises strain comparison of un-patched (L) and patched (R) crack tips during the early stage of crack blunting

through the neutral axis of the patch repaired specimen. This causes the surface strain of the composite patched specimen to increase at a greater rate.

Once the load axis aligns with the neutral axis of the specimen both the un-patched and patched strain magnitudes are similar. Strain contours for a COD of 0.2 mm, which is during the early stage of crack blunting, are shown Fig. 7.7. High strain for the un-patched specimen is focused at the crack tip with strains an order of magnitude lower near the specimen edge in line with the initial crack plane. This is due to a significant effect from bending as the region ahead of the crack tip deforms plastically. Strain contours for the patched specimen indicate a measureable effect of the surface reinforcement with a blunted region of high strain ahead of the crack tip and a larger area of aluminum exhibiting high strain ahead of the crack tip. The surface reinforcement in both axial and transverse directions effects the formation of the through thickness strain gradient ahead of the crack tip, which increases the size and shape of the region of aluminum supporting high strains and the area on the surface exhibiting plastic deformation. As previously discussed, this change in the formation of the plastic zone is most likely responsible for the 20% increase in COD when comparing specimen response at matching load levels after the patch fails.

## 7.5 Finite Element Model

Numerical predictions for the small scale specimen response were performed using a Finite Element Model (FEM) in the commercial software ABAQUS. The extended finite element method (XFEM) was utilized to define the crack and perform calculations of strain energy release rate at the crack tip and the J-integral around element defined paths ahead of the crack tip. Reduced integration linear brick elements (C3D8R) elements were used for all materials and the crack plane was defined by the built-in XFEM method to split the solid elements [30]. The model was loaded in axial tension using nodal displacement control with only the surface nodes in the grip regions being displaced in the Y-direction. Displaced nodes were free to move in the X and Z directions to minimize nodal stress concentrations at the applied boundary conditions. Large displacement formulation was used to account for non-linear geometry due to bending from the asymmetric reinforcement when possible; limitations for J-integral calculation methods will be discussed later. Best practices were followed for the number of elements

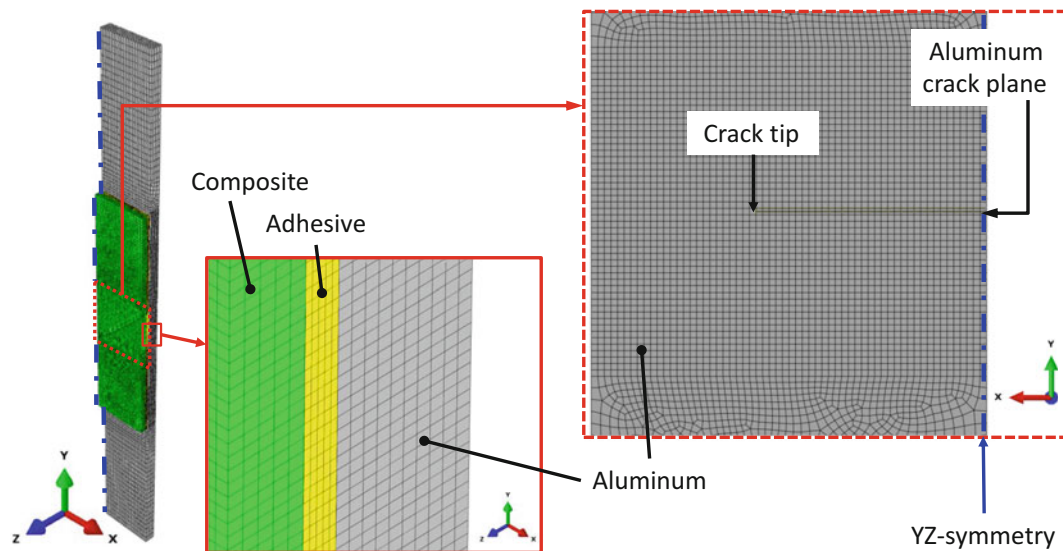


Fig. 7.8 Half symmetric finite element model element configuration details

through the thickness and ahead of the crack tip while maintaining element aspect ratios as close to 1 as possible. A minimum of 5 elements through the thickness is recommended to capture through thickness behavior, and based on previous work to capture the strain gradient necessary to capture fatigue crack growth a minimum of 0.5 mm elements along the crack path was adequate [12]. The resulting finite element model (FEM), shown in Fig. 7.8, had 10 elements through the thickness for the aluminum and 5 elements through the thickness for both the adhesive layer and the composite patch. Elements adjacent to the crack plane are 0.2 mm long (X) and 0.196 mm high (Y). Element thicknesses in the Z-direction vary; Aluminum elements are 0.226 mm thick, adhesive elements are 0.112 mm thick, and composite patch elements are 0.254 mm thick. The resulting element aspect ratios range from 0.56 to 1.30 in the region around the crack.

Two methods were used to calculate the J-integral using built-in XFEM processing methods. The basic method uses the virtual crack closure technique (VCCT), which is based on LEFM, local element based crack geometry, and nodal forces. Output from VCCT is the strain energy release rate (G), which for linear elastic material is equivalent to the J-integral ( $G = J$ ). This method does not capture non-linear behavior of the strain energy release rate as the material deforms plastically ahead of the crack tip. True J-integral behavior must be captured using Eq. 7.1, which when using ABAQUS XFEM is solved using the domain integral method [30]. The limitation with this method is that analysis steps are limited to small-displacement linear steps, which can capture material non-linearity but not geometric non-linearity due bending and limited ability to capture displacement due to elastic-plastic material behavior.

## 7.6 Material Properties

Constituent properties for each material used to manufacture the CCT specimens were independently verified by mechanical testing. Test data and the material behavior approximation used in the FEA are listed and shown in Fig. 7.9. Aluminum tensile properties were measured following ASTM E8 [31] testing guidelines using an ASTM E466 [32] sheet type specimen and compared against existing data [33]. Aluminum properties were averaged for four specimens with resulting modulus of  $70.9 \pm 0.9$  GPa, 0.2% offset yield strength of  $116 \pm 1$  MPa, and Ramberg-Osgood parameters  $\alpha$  and  $n$  of  $9.9 \pm 0.9$  and  $0.22 \pm 0.06$  respectively. WestSix10 adhesive tensile dog-bone and thick adhesive shear properties were measured following ASTM D638 and D5656 test standards [34, 35]. A total of six specimens were tested with resulting modulus of  $2.4 \pm 0.1$  GPa and a 0.2% offset yield strength of  $23.6 \pm 2.7$  MPa. Only linear elastic behavior was utilized for the current FEA. A total of six composite dog-bone specimens were tested in tension following ASTM D638. The resulting average modulus was  $22.2 \pm 1.2$  GPa and an average ultimate strength of  $300 \pm 4$  MPa.



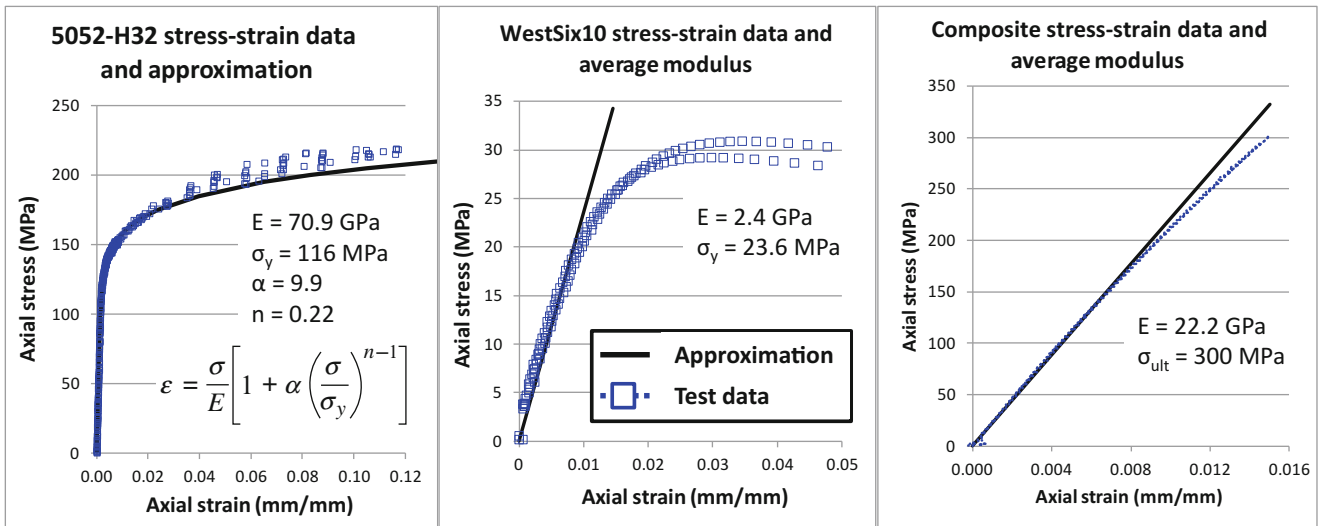


Fig. 7.9 Test data and behavior approximation for aluminum (L), adhesive (M), and composite (R) materials

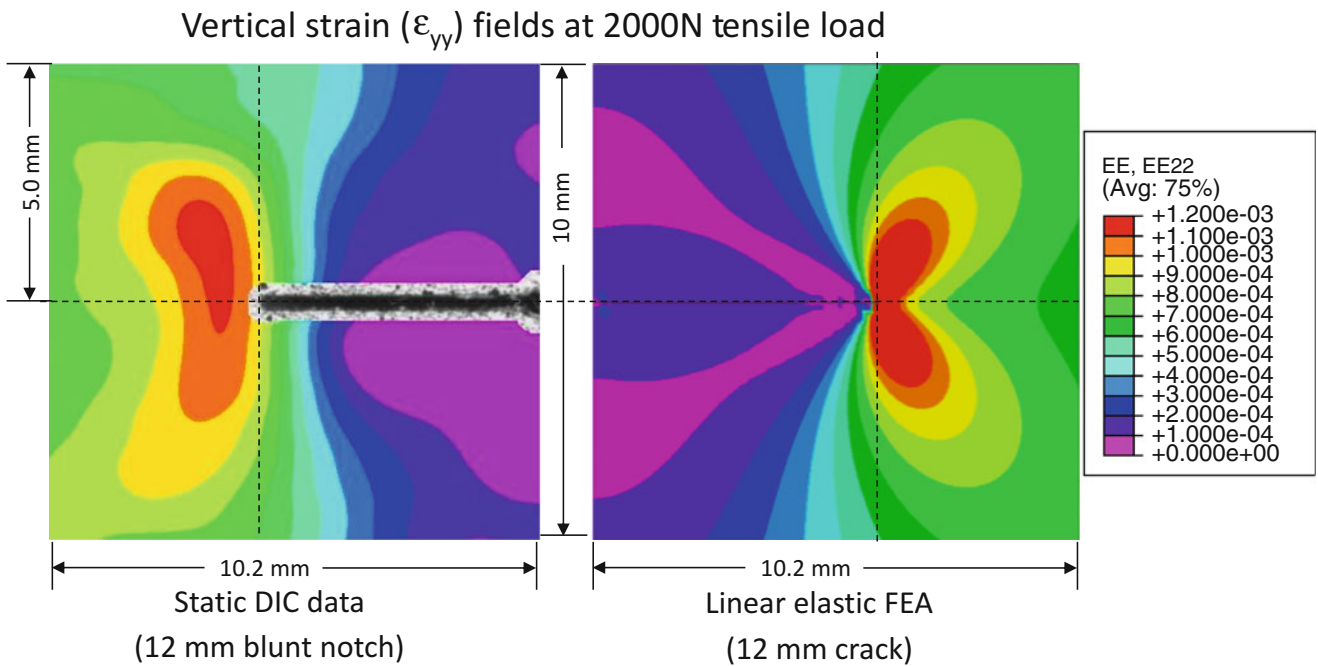


Fig. 7.10 Surface vertical strain: DIC (L) and FEA prediction (R)

### 7.7 Comparison of Test Results and Predictions

Comparison of the finite element analysis (FEA) predicted surface axial strain ( $\epsilon_{yy}$ ) and the DIC measured axial strains shown in Fig. 7.10 occurs at a load of 2000 N, which is at the edge of the linear elastic response. Strain magnitude and distribution for the DIC measured (L) and FEA predicted (R) correlate well. Though not shown here the vertical displacements also correlate well in the linear elastic range. The key difference between data and FEA prediction is the crack tip geometry. In the FEM the crack has a sharp tip defined by an infinitesimal plane while in reality the crack is a blunt 12 mm long EDM cut notch ( $2a$ ) prior to fatigue crack growth. Any effect the true notch geometry has on local strain behavior is not captured by the FEM.

Both LEFM and EPFM predictions for the J-integral value are shown in Fig. 7.11. LEFM solutions approximate the relationship between far-field stress and the plane stress crack tip stress intensity ( $K_I$ ), in Eq. 7.4 where P is the load, B is the aluminum thickness, W is the half width, and a is the half crack length. The finite geometry effect is accounted for using the

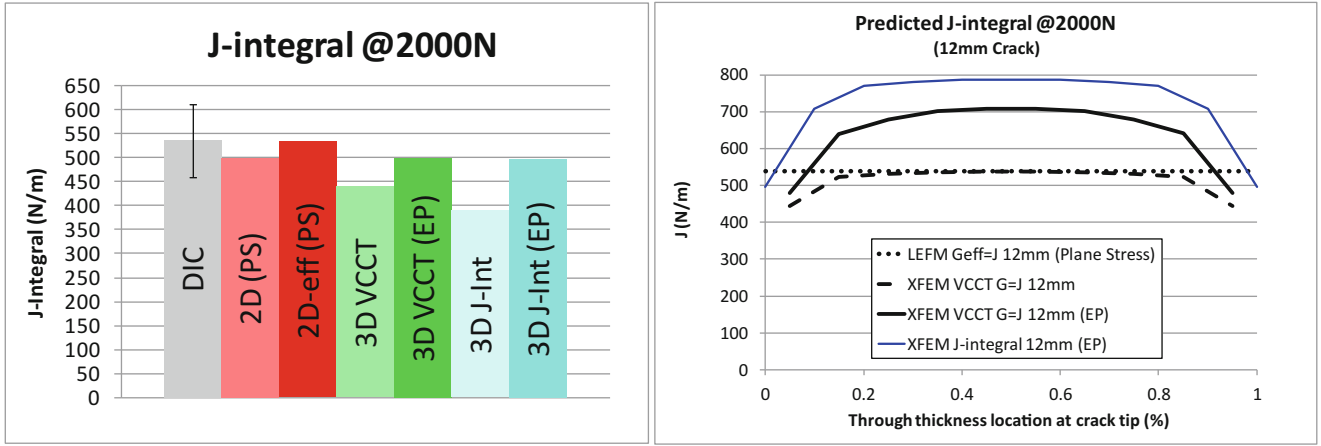


Fig. 7.11 Un-patched specimen DIC data and predictions for 2000 N load on the surface (L) and through the thickness (R)

correction factor in Eq. 7.5 [17] as well as an effective crack length to account for possible small scale first order plasticity at the crack tip in Eq. 7.6. Stress intensity is then converted to plane stress strain energy release rate with the plane stress relationship. Results for the 2D plane stress (2D PS) and effective J-integral (2D-eff PS) are shown in Fig. 7.11.

$$K_I = \frac{P}{B\sqrt{W}} f^{(a/w)} \quad (7.4)$$

$$f^{(a/w)} = \sqrt{\frac{\pi a}{4W}} \sec\left(\frac{\pi a}{2W}\right) \left[ 1 - 0.025\left(\frac{a}{W}\right)^2 + 0.06\left(\frac{a}{W}\right)^4 \right] \quad (7.5)$$

$$r_y = \frac{1}{2\pi} \left(\frac{K_I}{\sigma_{ys}}\right)^2 \quad a_{eff} = a + r_y \quad (7.6)$$

FEA predictions using VCCT and domain integral calculations are also included for a load of 2000 N. Results show that accounting for small scale plasticity in the J-integral value is necessary, by either using an effective crack length or including elastic-plastic material behavior. When including elastic-plastic behavior the predictions correlate well with DIC calculated J-integral values with predictions within 8% of the data.

Out of plane bending caused by the composite patch changes the through thickness distribution of SERR and strain, as shown in Fig. 7.12. J-integral value predictions, in the linear elastic range, correlate well with the measured value. From ABAQUS, the LEFM VCCT values are elemental values output at the centroid for the reduced integration elements used, while the domain integral is calculated on the element surfaces. Linearly extrapolating the LEFM results, the J-integral value for both prediction methods are within 5% of each other and 10–15% of the mean DIC value. At a load of 2000 N, the end of the linear elastic response, numerical prediction methods start to diverge in both magnitude and through thickness behavior.

The measured and predicted load versus COD behaviors shown in Fig. 7.13 focus on the COD before crack growth and material failure occur; when COD is less than 0.25 mm. For the un-patched specimens physical response is captured when accounting for elastic-plastic behavior of the aluminum. Patched predictions diverge from test data as loading proceeds through the crack blunting stage. Patched FEA is run two ways to get LEFM and EPFM predictions for the J-integral. First, for the LEFM VCCT prediction the model utilizes the non-linear geometry option in ABAQUS for the implicit solution incrementation, meaning equilibrium is solved for between successive analysis increments and accounts for bending that exists due to the asymmetry created by the one sided composite patch. This method over predicts the global stiffness of the non-linear response as COD increases past 0.10 mm; The FEM does not account for the non-linear shear behavior of the explicitly modeled adhesive layer. Then, for the EPFM domain integral method the FEA solution is restricted to linear geometry incrementation, which means that equilibrium is solved for between the initial configuration and the target end displacement or boundary condition for that step. Though both procedures account for non-linear material behavior the nodal displacement as elastic-plastic behavior occurs was over predicted with linear geometry increments. Linear geometry solutions typically result in a stiffer response with higher stress, which with elastic-plastic material behavior results in more strain and displacement per solution increment. Both predictions produce reasonable correlation when COD is less than 0.15 mm.

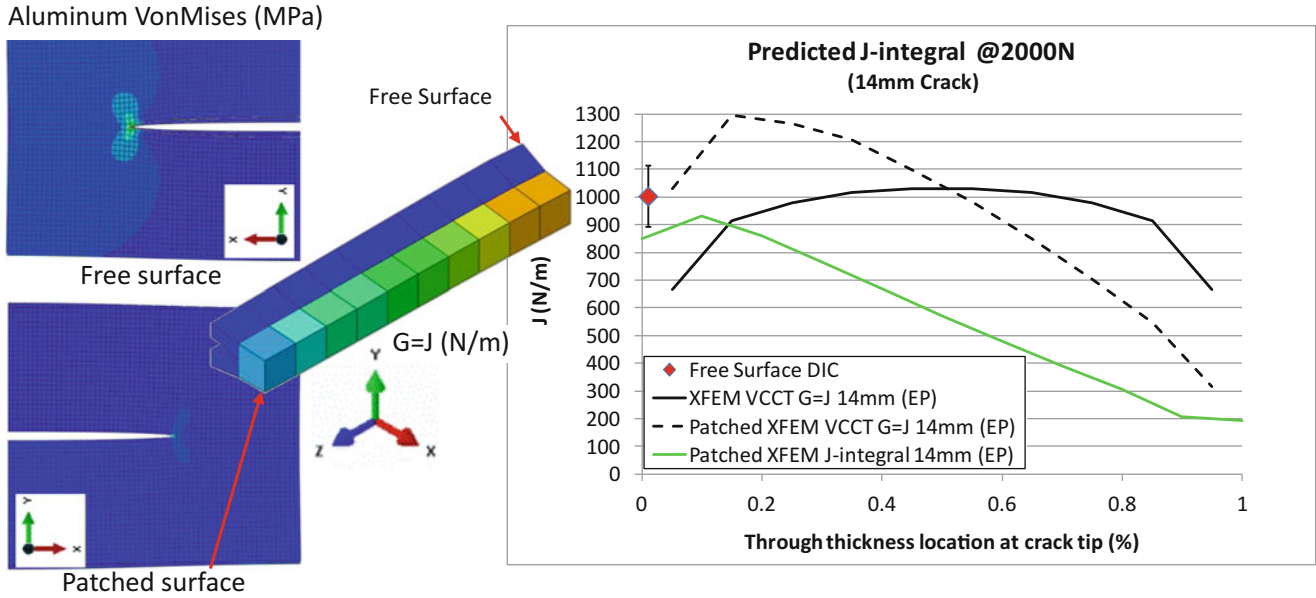


Fig. 7.12 Patched specimen DIC data and predictions of J-integral at 2000 N load

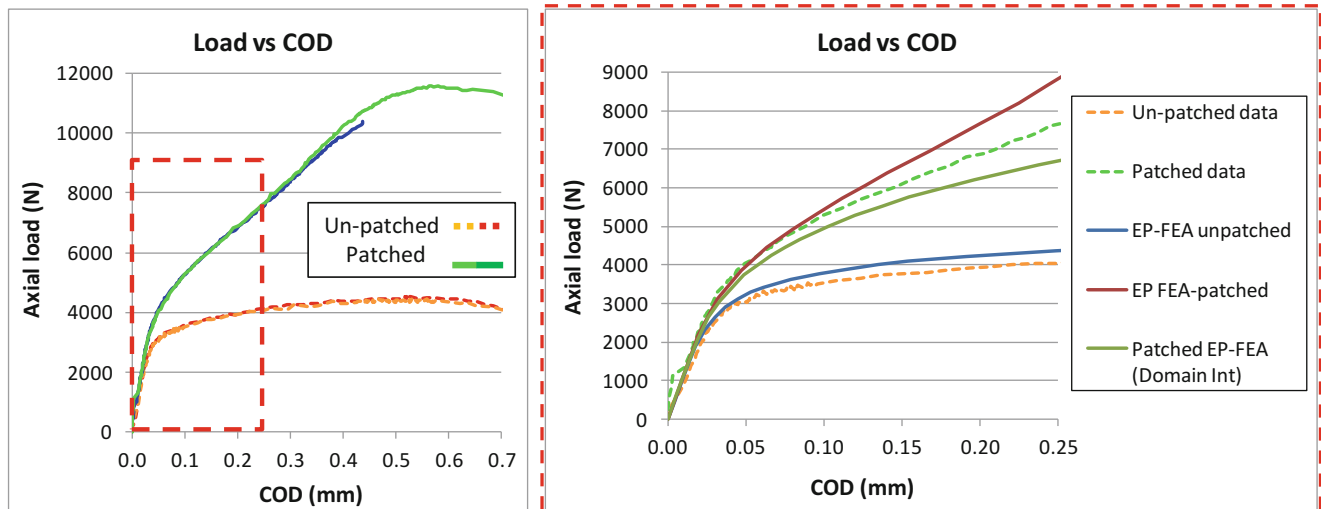


Fig. 7.13 Load versus COD predictions and test data early in the crack blunting stage with COD less than 0.25 mm

With the global specimen response correlating reasonably well, one can compare the J-integral value predictions. The COD response as a function of the J-integral value for COD magnitudes less than 0.25 mm is shown in Fig. 7.14. As shown with the un-patched and patched strain response, the free surface material response is nominally an intrinsic property of the aluminum, that as a function of COD shows negligible variation with surface reinforcement. Though the patched response requires more load to achieve the same COD, similar behavior is observed when the J-integral value on the surface is related to COD. The key finding here is the amount of divergence between LFM and EPFM J-integral predictions as load and COD increases beyond the linear elastic response. FEA under predicts the COD as a function of the J-integral value, meaning that at a given COD the analytical procedure required to calculate the domain integral predicts a lower load and more strain than measured. Over predicting the strain results in a higher strain energy release rate, or J-integral value, than measured.



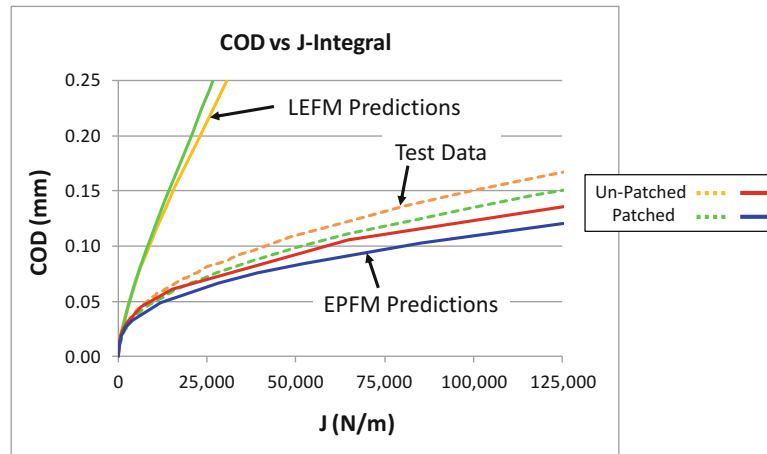


Fig. 7.14 COD versus J-Integral for test data and FEA

## 7.8 Conclusions

Using full field DIC test data and FEA the influence one sided composite patch reinforcement has on the free surface local crack tip elastic-plastic behavior was studied. Un-patched and patched CCT specimen response to a far field tensile load was both measured and predicted. Monotonic tensile loading until failure demonstrated a greater than 100% increase in ultimate failure load of the patched versus un-patched specimen. Composite patch reinforcement increases the ability of the specimen to carry more tensile load due to the load transfer to the patch, however testing demonstrated behavior on the free-surface ahead of the crack tip appears to remain an intrinsic material property independent of the patch. Both strain and J-integral behavior on the free surface until the end of the crack blunting stage was independent of the specimen configuration, un-patched or patched, when related to the COD. The bending deformations and plastic zone formation ahead of the crack tip induced by the patch did appear to affect crack-tip blunting, which resulted in a 20% increase in COD at a given load level after patch failure.

Both analytical and numerical predictions of load versus COD and J-integral values correlated well with test data in the linear elastic response range. As loading and COD increase beyond the linear elastic response and elastic-plastic material behavior begins to occur, LEFM and EPFM predictions diverge. ABAQUS was used to numerically predict specimen response and J-integral values two ways with different implicit solution methods. The LEFM based VCCT method under predicts the J-integral value beyond the linear elastic response, but accounts for the non-linear response due to bending and elastic-plastic material behavior by solving for equilibrium between each solution increment and automatically sizing the increment. The EPFM predictions are currently limited to finite displacement solution increments that solve for equilibrium between the initial and current state with no automatic step sizing, which results in the over prediction of displacements and strains.

Testing and analysis results will guide future efforts. Comparing test response to the predicted response indicates a few mechanisms still need to be accounted for in the numerical predictions. Un-patched and patched specimen strain response indicates that accounting for the elastic-plastic shear behavior of the adhesive may be required to improve correlation. To fully capture the load response and the J-integral value requires a post processing method to extract surface displacements from an analysis that allows equilibrium solutions between increments. Extracting surface displacements can then be used to perform the J-integral calculation on arbitrary paths about the crack tip. Further improvements in the J-integral correlation can be achieved by including the elastic-plastic stress-strain material behavior at the crack tip as included in methods described by Hickey, Yoneyama et al., and Becker et al. [23–25].

**Acknowledgements** Work described was performed by the Naval Surface Warfare Center Carderock Division's Survivability, Structures, Materials Department, and University of Maryland College Park's Mechanical and Reliability Engineering department. Financial and technical support was provided by an NSWCCD In-house Laboratory Independent Research (ILIR) program under Dr. Jack Price, and a grant provided to UMD by program officer Dr. Paul Hess of the Office of Naval Research Code 331 under grant number N000141612351.

## References

1. Volkersen, O.: Die Niektraft in Zugbeanspruchten mit Kontanten Laschenquerschriften. *Luftfahrtforschung*, **5**, 41–47 (1938)
2. Goland, M., Reissner, E.: The stress in cemented joints. *J. Appl. Mech.* **77**, (1944)
3. Hart-Smith, L.J.: Adhesive-Bonded Double-Lap Joints, CR-112235, NASA, (1973)
4. Hart-Smith, L.J.: Adhesive-Bonded Single-Lap Joints, CR-112236, NASA, (1973)
5. Sabelkin, V., Mall, S., Avram, J.B.: Fatigue crack growth analysis of stiffened cracked panel repaired with bonded composite patch. *Eng. Fract. Mech.* **73**, 1553–1567 (2006)
6. Schubbe, J.J., Mall, S.: Investigation of a cracked thick aluminum panel repaired with a bonded composite patch. *Eng. Fract. Mech.* **63**, 305–323 (1999)
7. Tsai, G.-C., Shen, S.B.: Fatigue analysis of cracked thick aluminum plate bonded with composite patches. *Compos. Struct.* **64**, 79–90 (2004)
8. Jones, R., Chiu, W.K.: Composite repairs to cracks in thick metallic components. *Compos. Struct.* **44**, 17–29 (1999)
9. Duong, C.N.: Design and validation of composite patch repairs to cracked metallic structures. *Compos. Part A*, **40**, 1320–1330 (2009)
10. Baker, A.A., Rose, L.R.F., Jones, R.: *Advances in the Bonded Composite Repair of Metallic Aircraft Structures*, vol. 1. Elsevier: Oxford (2002)
11. Noland, J.M., Hart, D.C., Udinski, E.P., Sielski, R.A.: Initiatives in bonded ship structural repairs. In *ASNE Fleet Maintenance and Modernization Symposium*. San Diego: American Society of Naval Engineers. Conference (2013)
12. Baker, A.A., Rose, L.R.F., Walker, K.E., Wilson, E.S.: Repair substantiation for a bonded composite repair to F111 lower wing skin. *Appl. Compos. Mater.* **6**, 251–267 (1999)
13. Muller, R., Fredell, R.: Analysis of multiple bonded patch interaction simple design guidelines for multiple bonded repairs in close proximity. *Appl. Compos. Mater.* **6**, 217–237 (1999)
14. Hart, D.C.: 5xxx Aluminum Sensitization and Application of Laminated Composite Patch Repairs. In: *Society for Experimental Mechanics XIII International Congress and Exposition on Experimental Applied Mechanics, Experimental Dynamic Behavior: Integrating Experimental Mechanics*. Orlando. Conference (2016)
15. Nahshon, K., Hoffman, W.A., Ullagaddi, C.B.: Characterization of structural scale ductile fracture of aluminum panels using digital image correlation. In: *Proceedings of the 2014 Annual Conference on Experimental and Applied Mechanics*. Conference (2014)
16. Hart, D.C., Udinski, E.P., Hayden, M.J., Liu, X.: Fatigue performance and analysis of composite patch repaired cracked aluminum plates. In: *Sustainability and Stewardship, Vessel Safety and Longevity Through Research*. Linthicum Heights: Ship Structures Committee. Conference (2014)
17. Anderson, T.L.: *Fracture Mechanics Fundamentals and Applications*, 2nd edn. CRC Press LLC: Raton (1995)
18. Hutchinson, J.W.: *A Course on Non-Linear Fracture Mechanics*. Department of Solid Mechanics, The Technical University of Denmark, Copenhagen (1979)
19. Rice, J.R.: *A Path Independent Integral and the Approximate Analysis of Strain Concentration by Notches and Cracks*, D.o.D.A.R.P. Agency, Editor (1967)
20. Sutton, M.A., Orteu, J.-J., Schreier, H.W.: *Image Correlation for Shape, Motion, and Deformation Measurements*. Springer, LLC: New York (2009)
21. Bruck, H.A.: Analysis of 3-D Effects near the Crack Tip on Rice's 2-D J-Integral Using Digital Image Correlation and Smoothing Techniques. In: *Department of Mechanical Engineering*. University of South Carolina, Columbia (1989)
22. Sutton, M.A., Turner, J.L., Chao, Y.J., Bruck, H.A., Chae, T.L.: Experimental investigations of three dimensional effects near a crack tip using computer vision. *Int. J. Fract.* **53**, 201–228 (1992)
23. Yoneyama, S., Arikawa, S., Kusayanagi, S., Hazumi, K.: Evaluating J-integral from displacement fields measured by digital image correlation. *Strain*, **50**, 147–160 (2014)
24. Hickey, W.F.: An investigation into the failure of aluminum alloys. In: *Material Science and Engineering*. University of Texas at Austin, Austin (2011)
25. Becker, T.H., Mostafavi, M., Tait, R.B., Marrow, T.J.: An approach to calculate the J-integral by digital image correlation displacement field measurement. *Fatigue Fract. Eng. Mater. Struct.* **35**, 971–984 (2012)
26. Fernandez Zuniga, D., Kalthoff, J.F., Fernandez Canteli A., Grasa, J., Doblare, M.: Three dimensional finite element calculations of crack tip plastic zones and KIC specimen size requirements. In: *European Conference on Fracture*. Stockholm: Engineering Structural Integrity Society. Conference (2004)
27. Hamam, R., Hild, F., Roux, S.: Stress intensity factor gauging by digital image correlation: application in cyclic fatigue. *Strain*, **43**, 181–192 (2007)
28. Golumbfskie, W.J.: Aluminum sensitization and the navy. In: *The Minerals, Metals, and Materials Society 143rd Annual Meeting and Exhibition*. San Diego, Conference (2014)
29. Golumbfskie, W.J., Tran, K.T., Noland, J.M., Park, R., Stiles, D.J., Grogan, G., Wong, C.: Survey of detection, mitigation, and repair technologies to address problems caused by sensitization of Al-Mg alloys on navy ships. *Corrosion*, **72**(2), 314–328 (2016)
30. V2016, A: *Software Users Manuals*. Dassault Systemes Simulia Corporation, Providence, RI (2015)
31. ASTM E8M-08: *Standard Test Methods for Tension Testing of Metallic Materials*. ASTM International, Conshohocken (2008)
32. ASTM E466-07: *Standard Practice for Conducting Force Controlled Constant Amplitude Axial Fatigue Tests of Metallic Materials*. ASTM International, Conshohocken (2007)
33. Ozturk, F., Toros, S., Kilic, S.: Evaluation of tensile properties of 5052 type aluminum-magnesium alloy at warm temperatures. *Arch. Mater. Sci. Eng.* **34**(2), 95–98 (2008)
34. ASTM D638: *Standard Test Method for Tensile Properties of Plastics*. ASTM International, Conshohocken (2003)
35. ASTM D5656: *Standard Test Method for Thick-Adherend Metal Lap-Shear Joints for Determination of the Stress-Strain Behavior of Adhesives in Shear by Tension Loading*. ASTM International, Conshohocken (2004)